Collisionless shock acceleration of protons in a plasma slab produced in a gas jet by the collision of two laser-driven hydrodynamic shockwaves

View Online   Export Citation   CrossMark

J.-R. Marquès,[1,a] L. Lancia,[1] P. Loiseau,[2,3] P. Forestier-Colleoni,[1,b] M. Tarisien,[4] E. Atukpor,[4]
V. Bagnoud,[5,6] C. Brabetz,[5] F. Consoli,[7] J. Domange,[4] F. Hannachi,[4] P. Nicolaï,[8]
M. Salvadori,[7] and B. Zielbauer[5]

AFFILIATIONS

[1] LULI, CNRS, École Polytechnique, CEA, Sorbonne Université, Institut Polytechnique de Paris,
 91128 Palaiseau Cedex, France
[2] CEA, DAM, DIF, 91297 Arpajon Cedex, France
[3] Université Paris-Saclay, CEA, LMCE, 91680 Bruyères-le-Chatel, France
[4] CENBG, CNRS-IN2P3, Université de Bordeaux, 33175 Gradignan Cedex, France
[5] GSI Helmholtzzentrum für Schwerionenforschung GmbH, Planckstraße 1, 64291 Darmstadt, Germany
[6] University of Darmstadt, Schloßgartenstr., 764289 Darmstadt, Germany
[7] ENEA Fusion and Technologies for Nuclear Safety Department, C.R. Frascati, Via Enrico Fermi 45, Frascati, Rome, Italy
[8] CELIA, Université de Bordeaux–CNRS–CEA, 33405 Talence, France

[a] Author to whom correspondence should be addressed: jean-raphael.marques@polytechnique.fr
[b] Present address: Université Paris-Saclay, CEA, LIDYL, 91191 Gif-sur-Yvette, France.

ABSTRACT

We have recently proposed a new technique of plasma tailoring by laser-driven hydrodynamic shockwaves generated on both sides of a gas jet [Marquès *et al.*, Phys. Plasmas **28**, 023103 (2021)]. In a continuation of this numerical work, we study experimentally the influence of the tailoring on proton acceleration driven by a high-intensity picosecond laser in three cases: without tailoring, by tailoring only the entrance side of the picosecond laser, and by tailoring both sides of the gas jet. Without tailoring, the acceleration is transverse to the laser axis, with a low-energy exponential spectrum, produced by Coulomb explosion. When the front side of the gas jet is tailored, a forward acceleration appears, which is significantly enhanced when both the front and back sides of the plasma are tailored. This forward acceleration produces higher-energy protons, with a peaked spectrum, and is in good agreement with the mechanism of collisionless shock acceleration (CSA). The spatiotemporal evolution of the plasma profile is characterized by optical shadowgraphy of a probe beam. The refraction and absorption of this beam are simulated by post-processing 3D hydrodynamic simulations of the plasma tailoring. Comparison with the experimental results allows estimation of the thickness and near-critical density of the plasma slab produced by tailoring both sides of the gas jet. These parameters are in good agreement with those required for CSA.

I. INTRODUCTION

Collisionless shocks are ubiquitous in astrophysical environments[1,2] such as the Earth's bow shock, solar flares, interplanetary traveling shocks, and supernova remnants (SNRs).[3,4] They are believed to be responsible for nonthermal particles[5,6] and gamma ray bursts.[7] Using scaling laws,[8] the physics of collisionless magnetized shocks in SNRs has been investigated experimentally

using laser-produced plasmas.[9,10] Their capability to accelerate particles has been demonstrated.[11]

The formation of a collisionless electrostatic shock requires the creation of a localized region of higher pressure within a plasma with electron temperature T_e much larger than the ion temperature T_i. As this region of high pressure (defined as the downstream region) expands, it can drive a shockwave into the surrounding lower-pressure plasma (defined as the upstream region). The shockwave front can accelerate upstream ions by reflecting them to twice the shock velocity if the shock potential is larger than the kinetic energy of the incoming ions in the shock-rest frame.

Being efficient accelerators of particles, laser-driven shocks have attracted growing interest as possible compact particle accelerators.[12–15] Energetic ion beams from compact laser-produced plasmas have potential applications in many fields of science and medicine, such as particle physics,[16] fast ignition of fusion targets,[17–19] materials science,[20] proton radiography,[21–23] radiotherapy,[24–27] and isotope generation for medical applications.[28,29]

Several schemes for laser-driven ion acceleration have been proposed: target normal sheath acceleration (TNSA),[30,31] radiation pressure acceleration (RPA),[32–35] and breakout afterburner acceleration,[36,37] all of which use over-dense targets (solid-density foils or liquid jets), and magnetic vortex acceleration (MVA)[16,38,39] and collisionless shock acceleration (CSA), both of which use near-critical-density (NCD) targets (exploded foils or gas jets). The production, at high repetition rate, of high-energy ion beams with a narrow energy spread and a low divergence still remains a challenge, and CSA could potentially offer these properties. Moreover, NCD plasmas can be generated using gas jets, offering several advantages (compared with other target types) such as the avoidance of target debris that usually spoil the surrounding optics, the avoidance of the target replacement and realignment between consecutive shots, and the ability to produce pure (impurity-free) proton beams by using H_2 gas.

Proton acceleration by CSA in a hydrogen gas jet was first demonstrated[15,40] using CO_2 lasers, the low critical density ($n_c \approx 10^{19}$ cm^{-3}) associated with their long wavelength ($\lambda_0 = 10$ μm) allowing the exploitation of regular-pressure, millimeter-scale gas jets. A proton beam of ~MeV energy was produced with narrow energy spread ($\sigma \sim 4\%$) and low normalized emittance (<8 nm rad). To date, the maximum proton energy produced by CSA in a gas jet[41] is 20 MeV. This was achieved with a CO_2 laser using several picosecond (ps) pulses, the early pulses serving to ionize the gas jet and to steepen the plasma density profile on the front side of the target by the radiation pressure of the laser, so that the following pulses interacted with a step-like density profile. Despite this promising proton acceleration, the pulse train, inherent to the laser system, varied from shot to shot, making the interactions challenging to reproduce. Instabilities such as laser filamentation and hosing from the leading pulses result in variable density profiles, which in turn lead to fluctuations in the resultant ion beam. One way to generate a steep plasma density profile in a more stable manner is to tailor the near-critical gas target by a hydrodynamic shockwave (HSW) excited before the arrival of the main ps pulse. This HSW can be excited by a low-energy laser prepulse that can be focused inside the gas jet,[42] or on a solid target placed at the entrance side of the jet.[43] In both cases, it has been demonstrated that for long density profiles (>40 μm), ion beams with broadband energy spectrum are produced, whereas for

shorter plasma lengths (<20 μm), quasi-monoenergetic acceleration of protons is observed.

Experiments with the more widely available solid state ps lasers ($\lambda_0 \approx 1$ μm, $n_c \approx 10^{21}$ cm^{-3}) have been performed using high-pressure narrow gas jets tailored by an HSW[44,45] or using exploded micrometer-size solid foils.[46,47] Compared with the proof-of-principle experiments with CO_2 lasers, the number of accelerated protons was substantially higher (~$10^4\times$), thanks to the larger n_c and vector potential of the laser field ($a_0 \sim 4$–25, vs ~1 on the CO_2 experiments). Proton beams with peaks at energies up to 5.5 MeV from tailored gas jets and 54 MeV from exploded foils have been obtained.

Despite the large differences in terms of laser or target types, this set of experiments showed that the shape and maximum energy of the ion distributions depend strongly on the profile and peak value of the plasma density. Ion beams with peaked energy distribution and similar velocity of ion species with different charge-to-mass ratios, consistent with CSA, were observed only for plasmas with a steep density gradient at the laser entrance side and of NCD. To obtain a narrow energy spread by CSA,[12–14] it is crucial to have a uniform shock velocity and ion reflection, which implies a uniform electron temperature profile, only achievable by a rapid recirculation of the heated electrons due to the space-charge fields at the front and at the back of the target. Therefore, the plasma width L should be limited, which for a moderate Mach number shocks ($M \gtrsim 1$), means $L_{opt} \sim \lambda_0 (m_i/m_e)^{1/2}$. Considering a hydrogen plasma and $\lambda_0 = 1$ μm yields $L_{opt} \sim 40$ μm, and therefore relatively sharp gradients on both sides of the target.

To generate such thin NCD plasmas, we recently proposed a new tailoring method[48,49] based on a narrow gas jet coupled with two parallel nanosecond (ns) heating lasers that propagate perpendicular to the main ps laser. These ns beams are focused on both sides of the gas jet. The sudden and localized ionization and heating occurring at their foci generate two cylindrical HSWs. The expansion of each wave has two effects: (i) the part that expands toward vacuum expels the wing of the gas jet, while (ii) the part propagating toward the center of the jet compresses the plasma. The collision at the jet center of the two waves generates a thin plasma slab with steep gradients. Our hydrodynamic and ion Fokker–Planck simulations indicated that with present high-density gas jets,[50] this method allows the production of a thin ($\gtrsim 10$ μm) plasma slab, with an adjustable density up to 2×10^{22} cm^{-3} (20n_c for a 1 μm laser). This tailoring scheme can be implemented at high repetition rate, in a debris-free environment, and with different types of gas. Such thin NCD targets have attracted attention recently not only for use in CSA or other ion acceleration mechanisms,[51] but also for brilliant gamma-ray and electron–positron pair production.[52–54]

In this paper, we present experimental results on proton acceleration in an H_2 gas jet laser-tailored by the technique proposed in our previous numerical work.[48,49] We study the influence of plasma tailoring on the energy and angular distributions of the accelerated protons, for three cases: without tailoring, by tailoring only the entrance side of the ps beam, or by tailoring both sides of the gas jet. We observe a transition from a transverse (to the ps beam direction) acceleration with a low-energy broad spectrum produced by Coulomb explosion to a forward acceleration with a higher-energy peaked spectrum, in good agreement with CSA. The spatiotemporal evolution of the plasma profile is characterized by optical shadowgraphy of a probe laser beam. This shadowgraphy is simulated by

a post-processing (ray-tracing) of three-dimensional hydrodynamic simulations of the plasma tailoring, and the simulated shadowgraphs are compared with experimental observations to estimate the size and density of the resulting plasma slab.

II. EXPERIMENTAL SETUP

The work was performed on two laser facilities, PHELIX at GSI (Germany) and PICO2000 at LULI (France), both delivering laser pulses at a fundamental wavelength $\lambda_0 \sim 1\ \mu$m. The experimental arrangement is sketched in Fig. 1. The plasma was generated from a narrow, high-density, supersonic jet of hydrogen gas expelled from a 250 μm output diameter nozzle. The two parallel ns beams for plasma tailoring were focused 300 μm away from each side of the jet center. The ps laser beam driving the proton acceleration propagated at 90° from the ns beams and focused at the center of gas jet. The output of the gas nozzle was placed 400 μm above the propagation plane of the ps and ns laser beams. In this plane, the gas density profile, measured by interferometry of a probe beam,[50] was fitted to $n_{\mathrm{atom}}(r)\ (\mathrm{cm}^{-3}\ \mathrm{bar}^{-1}) \sim 6.2 \times 10^{17} \{\exp[-(r/186)^2] + 0.63 \exp[-(r/132)]\}$. The backing pressure was adjustable up to 1000 bars, allowing, without laser tailoring, a density of $n_e \sim n_c$ to be reached, where the critical plasma density $n_c\ (\mathrm{cm}^{-3}) \sim 1.11 \times 10^{21} \lambda_0^{-2}\ (\mu m)$.

The ps beam had an energy of ~25 J at GSI and ~50 J at LULI. It was focused to a Gaussian-like focal spot of 10 μm FWHM (in intensity). The temporal profile was Gaussian with full widths at half maximum (FWHM) of 0.5 ps at GSI and 1 ps at LULI, and contrasts on the ns scale (amplified stimulated emission, ASE) of 10^{11} and 10^7, respectively. The peak intensities were 8×10^{19} and 2×10^{19} W cm^{-2}, respectively, corresponding to normalized vector potentials of $a_0 \sim 8$ and 4. The Rayleigh length of the ps beam was $z_R \gtrsim 250\ \mu$m,

of the order of or greater than the width of the gas jet. The ns beams had square-like temporal profiles of ~1 ns duration. Each ns beam was focused to a spot of FWHM ~67 μm (GSI) and 42 μm (LULI), containing up to 15 and 6 J, respectively.

In both experiments, the hydrodynamic evolution of the plasma was controlled by two-dimensional (2D) shadowgraphy and interferometry of a probe laser beam of 0.5 μm wavelength propagating at 90° with respect to the ps beam and parallel to the ns beams. This probe beam was collimated, with a diameter covering the entire interaction region. At GSI, it was generated by the leakage of a dielectric mirror in the ps-beam path, sent to a delay line, and frequency-doubled, leading to a jitter-free probe of 0.5 ps duration. Its transverse intensity (shadowgraphy) and phase (interferometry) profiles at the exit of the plasma were recorded on 16-bit CCD cameras. The probe beam at LULI had a Gaussian temporal profile of FWHM ~7 ns. The shadowgraphy and interferometry at a given time (snapshot) were recorded on a gated optical intensifier (GOI) coupled to 16-bit CCD cameras, with an integration window of 100 ps. The shadowgraphy profile along the ps-beam axis was imaged on the entrance slit of a streak camera, with a time resolution of 100 ps. The long duration of the probe beam enabled the propagation of the shockwaves to be followed from their creation to their collision, and thus allowed checking and adjustment of the synchronization of the HSW collision with the arrival of the ps beam. The time jitters of the GOI and of the streak camera diagnostics were less than 50 ps. The shadowgraphy and interferometry diagnostics used the same collecting lens, with an angular aperture of ±3.5° at LULI and ±2° at GSI, leading to a spatial resolution better than 10 μm. The focal spots of the ns beams were recorded on a 12-bit CCD, which allowed their adjustment on both sides of the gas jet before shot, as well as control of their positions, shapes, and transmitted energies on shot. The position of the ps beam was controlled before shot on an 8-bit CCD. In addition to these "side-view" diagnostics (shadowgraphy, interferometry, and focal spots), the interaction region was also imaged from the "bottom" on a 12-bit CCD. The second-harmonic light (0.5 μm) emitted by the ps beam along its propagation in the plasma was recorded on the "side-view" and "bottom-view" diagnostics, allowing identification of the regions where the density gradients or the laser intensity were high, or where beam refraction or self-focusing could occur. The energy spectra of the protons accelerated from the H_2 plasma were recorded on image plates (Fuji BAS-MS type) coupled to magnetic spectrometers. In the LULI experiment, these were positioned at 0°, 30°, and 70° from the ps-laser axis and at 56, 47, and 30 cm, respectively, from the laser focus. In the GSI experiment, they were at 25°, 37°, and 53° and at 49, 114, and 107 cm, respectively. A pinhole of 500 μm diameter was placed at the entrance of each spectrometer, providing an energy resolution of 0.15 MeV, except for the spectrometer at 70° on the LULI experiment, where it was 0.075 MeV.

III. INTERACTION WITHOUT PLASMA TAILORING

Figure 2 shows 2D space-resolved shadowgraphs (snapshots) of the plasma generated by the interaction of the ps beam with the high-density H_2 gas jet, at different backing pressures and times for the LULI and GSI ps beams. At 800 bars [Figs. 2(a) and 2(c)], the expected peak density on the laser axis, assuming full ionization,
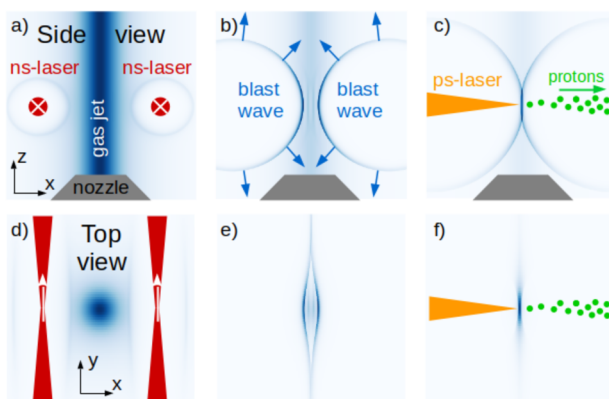

FIG. 1. Sketch of the experimental arrangement. (a)–(c) Side view (from the y axis) of the gas jet (blue column), that exits the nozzle along the z axis. (d)–(f) Top view (from the z axis). The two synchronized, ns beams (red) propagate parallel to the y axis, on both sides (x axis) of the gas jet. The sudden laser heating of the plasma induces steep density fronts [(a) and (d)] that propagate out of the laser axis as blast waves [(b) and (e)]. The collision of two blast waves at the center of the gas jet [(c) and (f)] produces a sharp-gradient, thin, high-density plasma slab. Protons are accelerated from the interaction of the ps pulse with the plasma.

is $n_e = 8 \times 10^{20}$ cm^{-3} ($0.8n_c$). Figure 2(a) shows that the plasma at $t = 0.2 \pm 0.1$ ns after the ps-pulse arrival is much larger than the laser focal volume and extends over the whole gas jet volume, on a millimeter scale, along the laser axis (x) as well as transversely (z). Shadowgraphs of very similar size and shape are observed at 450 bars [Fig. 2(b)] in the LULI experiment, as well as in the GSI experiment [Fig. 2(d)], for which the probe pulse is shorter (0.5 ps) and the pump pulse has a 10^4 times better ASE temporal contrast. The millimeter scale of these shadowgraphs is significantly larger than the FWHM of the gas jet, ~270 μm at $z = 0$, which will be discussed in Sec. VI. The prompt and localized energy deposition of the ps pulse along its

propagation leads to strong ponderomotive and thermal pressures, which transversely expel the plasma from the laser axis, as observed in Fig. 2(c), 1.7 ns after the ps pulse.

Time-resolved (streak camera) shadowgraphs along one dimension in space [the ps-beam axis (x, for $z = 0$)], are presented in Fig. 3 for two gas jet pressures. Despite the factor two difference in pressure, these shadowgraphs are very similar. For $t < 0$, the probe beam is undisturbed, indicating that the ASE contrast is high enough to avoid ionization of the gas before the ps-pulse arrival. For 0 ns < t < 1 ns, the shadowgraph extends symmetrically from the focal position up to $x \sim \pm 400$ μm, as observed on the snapshots in
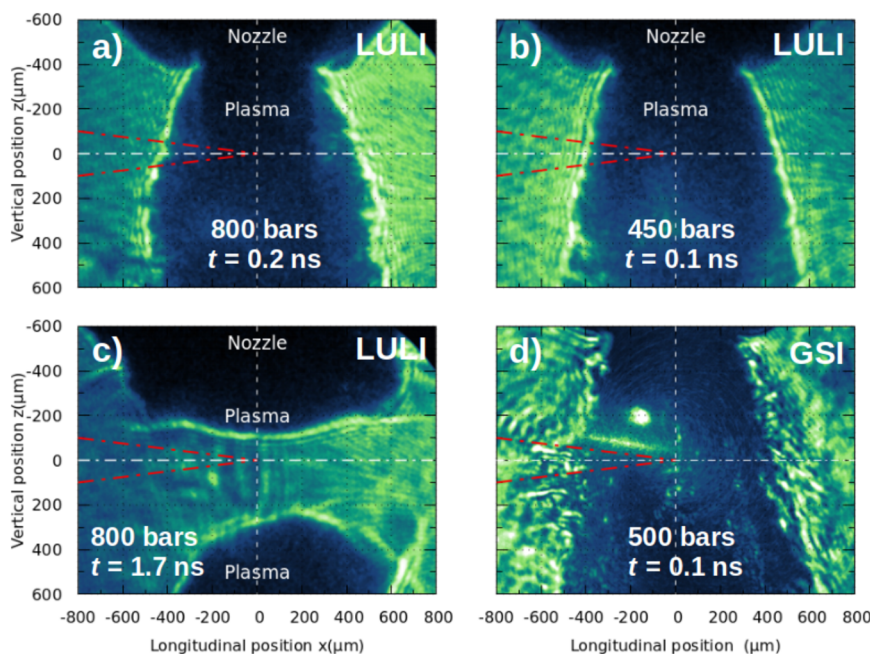

FIG. 2. Probe beam shadography from the plasma generated by the interaction of the ps beam with the high-density H$_2$ gas jet, at different backing pressures and different times from the ps-pulse arrival: (a)–(c) LULI experiment; (d) GSI experiment. At the top of each image ($z < -400$ μm) is the shadow of the nozzle. The ps beam propagates at $z = 0$ from left to right along the x axis (horizontal white dashed line), and is focused (red dashed lines) at the center of the jet ($x = 0$, $y = 0$). The vertical scale is the same for all four images.
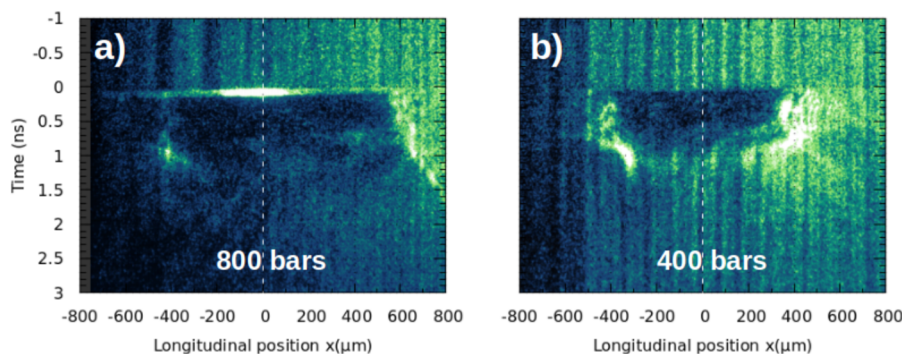

FIG. 3. Time-resolved (streak camera) shadowgraphs along the ps-beam axis (x, at $z = 0$), for two gas jet pressures. The ps pulse arrives at $t = 0$ and propagates from left to right as in Fig. 2. The vertical scale is the same for both images.

Figs. 2(a) and 2(b). At these edges, on applying the expression for the gas jet density given in Sec. II, the plasma density for the 800 bar case [Fig. 3(a)] is ~2 × 10^{19} cm^{-3} (0.02n_c). The bright line observed in Fig. 3(a) at $t = 0$, near the gas jet center ($-200\,\mu m < x < +100\,\mu m$), is the second-harmonic emission produced by the ps pulse, usually occurring in regions of strong laser intensity and/or density gradients. For $0\,ns < t < 1.5\,ns$, the longitudinal expansion of the right edge of the plasma ($x > 500\,\mu m$) can be observed. At $t \gtrsim 1\,ns$, the plasma expulsion induced by the ponderomotive and thermal pressures has lowered the density on the laser axis, and parts of the probe beam start to be transmitted again. As in Fig. 2(c), at $t \sim 1.7\,ns$, the plasma has been expelled from the laser axis, and the probe beam is no longer disturbed.

Proton spectra from the LULI experiment, measured at 0°, 30°, and 70° from the laser axis, are presented in Fig. 4 for the same laser-plasma parameters as in Figs. 2 and 3. The noise spectra (dashed lines) are obtained from the same analysis as for the proton spectra (solid lines), but applied to a region close to the dispersion zone but unexposed to protons. Even when the signal-to-noise ratio is low, the proton spectrum can be easily distinguished from the noise that exhibits a constant shape. Figure 4 shows that by directly focusing the laser on the gas jet, without plasma tailoring (no ns beams), the acceleration along the laser axis is very weak (if not zero), is larger at 30°, and much more efficient at 70°, almost perpendicularly to the laser axis. The spectrum has two components: an exponential part at low energy, followed by a plateau, extending up to 2 MeV at 70°. Such an energy distribution could be the result of "Coulomb explosion": ions are accelerated by electrostatic forces caused by charge separation induced by the laser ponderomotive pressure in the underdense part of the plasma.[49,55,56] The ponderomotive force is mainly transverse, and so the emission angles of the accelerated protons are centered around 90°. The maximum energy that can be gained is the relativistic ponderomotive energy $U_p = m_e c^2 (\gamma - 1)$, where $\gamma = (1 + a_0^2/2)^{1/2}$ is the relativistic factor of the electron quiver motion in the laser field. For the LULI experiment, $a_0 \sim 4$, leading to $U_p \sim 1$ MeV, which seems be too low to explain the high-energy part of the spectra. In addition, the ponderomotive energy depends only on the laser intensity, while the maximum energies observed

at 0°, 30°, and 70° seem to increase with the plasma density. The plateau structure, the maximum energy value, and its increase with the plasma density could be the signature of an acceleration by multiple collisionless shocks formed at high density.[12,57]

The shot-to-shot fluctuations of the proton spectra are attributed to the excitation of the filamentation instability that breaks the laser beam in the low-density part of the plasma profile.[49] The laser pulse loses its integrity and splits into filaments with different intensities and propagation angles from shot to shot.

IV. INTERACTION WITH A FRONT-FACE TAILORED PLASMA

1D time-resolved (streak camera) and 2D space-resolved (GOI snapshot) shadowgraphs of the plasma tailored by one ns beam at the entrance side of the ps beam are presented in Figs. 5(a) and 5(b), respectively, for a gas pressure of 200 bars. The ns pulse was sent into the gas jet ~2.7 ns before the ps pulse. It propagated along the y axis (perpendicular to the image plane) and focused at $x = -300\,\mu m$, $z = 0$ [red circle in Fig. 5(b)]. The lower backing pressure used for this tailoring case (200 bars, instead of 800 bars without tailoring) was chosen to avoid the ns-beam refraction at the jet entrance and for better plasma expulsion by the HSW, while preserving the high density at the jet center thanks to the density jump (compression) induced by the HSWs,[48] $(\gamma + 1)/(\gamma - 1)$, where γ is the heat capacity ratio of the gas. With $\gamma = 1.4$ for hydrogen, the density at the shock front could reach six times the background density.

The hydrodynamic evolution (on the ps-beam axis) of the plasma can be followed in Fig. 5(a). For $t < -2.5\,ns$, the probe beam is fully transmitted, indicating no pre-plasma. At $t \sim -2.7\,ns$, the ns beam promptly ionizes and heats the edge of the gas jet. A hydrodynamic shockwave is generated, which starts to push the plasma out of the ns-beam axis. At $-2.7\,ns < t < -2.3\,ns$, one can observe the plasma motion toward vacuum ($x < -300\,\mu m$) and toward the jet center ($x > -300\,\mu m$). At later times, the plasma moving toward vacuum becomes too tenuous to produce a shadow, while the HSW propagating toward the jet center stays dense and can easily be followed. In contrast to the ps-pulse interaction, which ionizes the
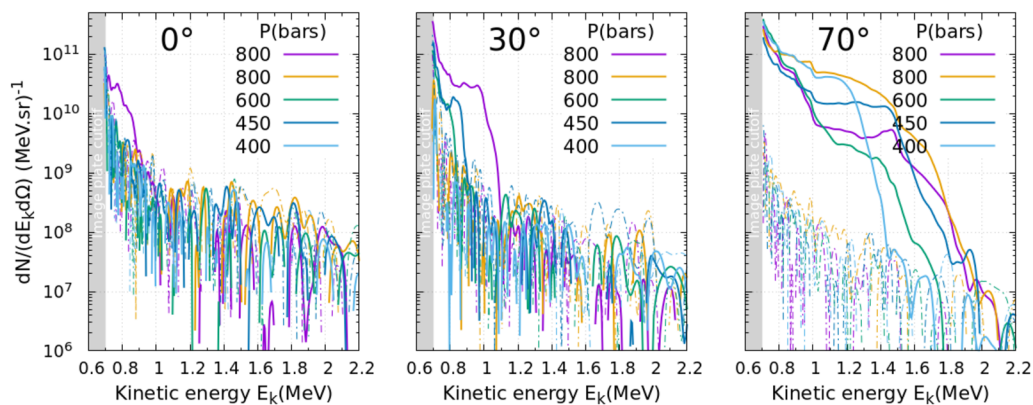

FIG. 4. Proton spectra from the LULI experiment, without plasma tailoring, measured at 0°, 30°, and 70° from the ps-beam axis, for different gas jet backing pressures. The dashed lines are the noise levels of each spectrum. The laser-plasma parameters are the same as in Figs. 2 and 3. The vertical scale is the same for all three graphs.
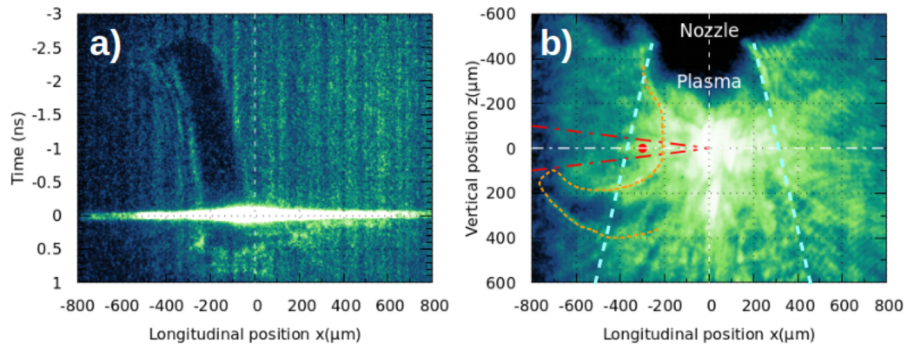
FIG. 5. (a) Time-resolved [along the ps-beam axis (streak camera)] and (b) 2D space-resolved (GOI snapshot) shadowgraphs of the plasma tailored by one ns beam, at the entrance side of the ps beam, for a gas jet backing pressure of 200 bars. The dashed orange line highlights the croissant-like shape produced by the expansion of the HSW [see also Figs. 7(b), 8, and 10(a)]. The ns pulse propagates along the y axis (perpendicular to the image plane) and focuses at $x = -300$ μm, $z = 0$ (red circle). It arrives in the gas jet ~2.7 ns before the ps pulse. The ps beam propagates at $z = 0$ from left to right along the x axis [horizontal white dashed line in (b)], and is focused [red dashed lines in (b)] at the center of the jet ($x = 0$, $y = 0$). The time integration window of the snapshot in (b) was ~120 ps, centered on the ps-pulse arrival.

whole gas jet volume very rapidly (Fig. 2), the ionization by the ns beam concerns only its focal region, the rest of the jet staying in the gaseous state until the arrival of the HSW (the right side of the jet stays undisturbed). The shockwave reaches the jet center at $t = 0$. At that time, the ps pulse arrives, crosses the plasma created by the HSW, and then interacts with the high-density non-ionized part of the gas jet (at $x = 0$), which induces strong second-harmonic emission that saturates the camera. The 2D plasma extension at that time can be observed in Fig. 5(b). The focal spot position of the ns beam is indicated by the red circle. The time integration window of the GOI was ~120 ps, centered on the ps-pulse arrival, and so the snapshot shows the plasma created by both the ns and ps beams, as well as the strong second-harmonic emission of the ps pulse. Partly hidden by this flash, a croissant-like shape can be distinguished [highlighted by the orange dashed line, and clearly visible in Figs. 7(b), 8, and 10(a)], which is the plasma generated by the expansion of the HSW. This initially cylindrical wave produces a circular shadowgraph that has evolved into a croissant-like shape because about half of the HSW expelled the plasma toward vacuum (left on the image), while the

part propagating toward the center of the jet ionized and compressed this high-density region. The horizontal extension of the croissant is larger on the bottom part of the image ($z > 0$) because of the conical shape of the gas jet (larger far from the nozzle exit). The blue dashed lines in Fig. 5(b) show the edges of the shadowgraph obtained for the case without tailoring [ps beam only, Figs. 2(a), 2(b), and 2(d)]. On the ns-beam side, the plasma has been pushed toward the jet center.

Proton spectra associated with the shadowgraphs of Fig. 5 are presented in Fig. 6. Tailoring the gas jet on the input side of the ps beam improves the forward acceleration. The maximum proton energies at 0° and 30° both increase, while the transverse (70°) acceleration becomes less efficient. In addition to the thermal exponential, the spectrum at 0° (Fig. 4) has a peaked component centered near 1.35 MeV. This indicates the appearance of another acceleration mechanism. Among the laser-driven ion acceleration schemes listed in Sec. I, CSA is the only one that in underdense or NCD plasmas is expected to produce a peaked energy spectrum, at twice the shock velocity. No acceleration (proton) was measured without the ps beam.
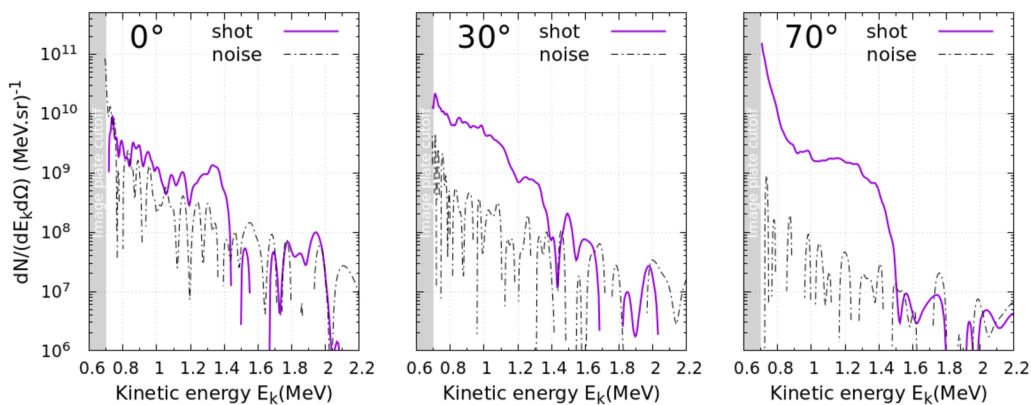

FIG. 6. Proton spectra from the LULI experiment, associated with the shadowgraphs of Fig. 5, for a plasma tailored at the entrance side of the ps beam. The vertical scale is the same for all three graphs.

V. INTERACTION WITH A FRONT- AND BACK-FACE TAILORED PLASMA

Examples of shadowgraphs of the plasma tailored on the two opposite sides are presented in Fig. 7. The ns beams arrive 2.5 ns before the ps pulse. At this time, we can see in Fig. 7(a) the prompt generation of the plasmas on both sides of the jet center, at the focal positions of the ns beams ($x = \pm 300$ μm), followed by the propagation of the HSWs. Only the dense parts converging toward the jet center are visible; the parts expanding toward vacuum are too tenuous to generate a significant shadowgraph. The central part of the jet stays in the gaseous state at least until $t \sim -1.4$ ns, when the shadowgraphs of each HSW start to overlap. The waves collide at the jet center at $t \sim -200$ ps, leading to a shadowgraphy with a minimum width of $\lesssim 300$ μm (orange arrows), slightly before the ps-pulse arrival ($t = 0$), visible by the second-harmonic emission it generates along its propagation (green line along the x axis). This width is much smaller than the one observed in Fig. 3 without plasma tailoring (~800 μm). As observed in Figs. 3(a) and 6(a), the ps pulse generates second-harmonic light at its arrival in the plasma. After that time, the collision of the HSWs has ended, and the plasma

starts to expand. At $t \sim 0.6$ ns, the strong ponderomotive and thermal pressures driven by the ps pulse have expelled the plasma from the laser axis, and the probe beam is transmitted again. A 2D space-resolved shadowgraph of the HSWs just before the ps-beam arrival is presented in Fig. 7(b). As already observed in Fig. 5(b), the initially cylindrical expansion of each HSW from the axis of its driving ns beam (red circles) has led to a croissant-like plasma of high density. The blue dashed lines in the figure indicate the edges of the shadowgraph measured without plasma tailoring (Fig. 2). This shows that tailoring the gas jet from the two opposite sides has allowed (i) a significant reduction in the plasma density at the edge of the gas jet and (ii) the generation of a high-density narrow (<300 μm) plasma slab along the ps-beam axis. This is also illustrated in Fig. 8 at a slightly higher pressure (300 bars), at two different times: before the collision of the HSWs [Fig. 8(a)] and just after their collision and the arrival of the ps pulse [Fig. 8(b)]. Before the ps-pulse arrival, the plasma is visible only at the location of the HSWs, whereas after its arrival, the region of the gas jet where the HSWs did not travel (bottom of the image, $z > 400$ μm) is promptly ionized, leading in this region to a broad shadowgraph comparable to the one observed without plasma tailoring (Fig. 2). On the opposite side, around the ns-beam
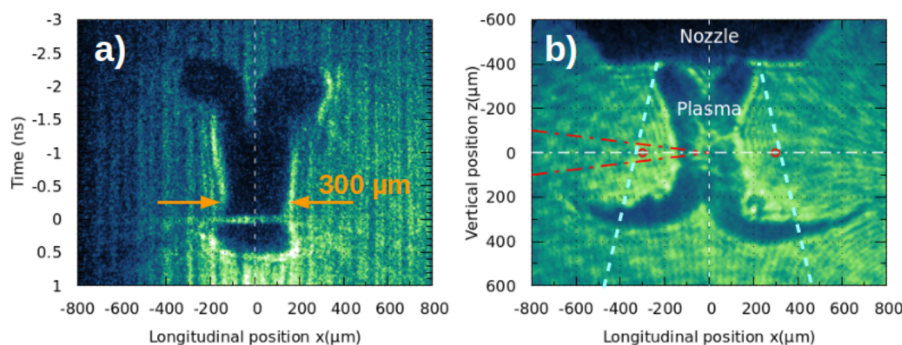

FIG. 7. (a) Time-resolved [along the ps-beam axis (streak camera)] and (b) 2D space-resolved (GOI snapshot) shadowgraphs of the plasma tailored on the two opposite sides for a gas jet backing pressure of 200 bars. The energy in each ns beam is 4.5 J. The orange arrows in (a) indicates the minimum width of the shadowgraph (collision of the two HSWs). The horizontal line at $t = 0$ is the second-harmonic emission of the ps pulse along its propagation (x axis). The time integration window of the snapshot in (b) was ~120 ps, ending just before the ps-pulse arrival. The blue dashed lines indicate the edges of the shadowgraph measured without plasma tailoring (Fig. 2).

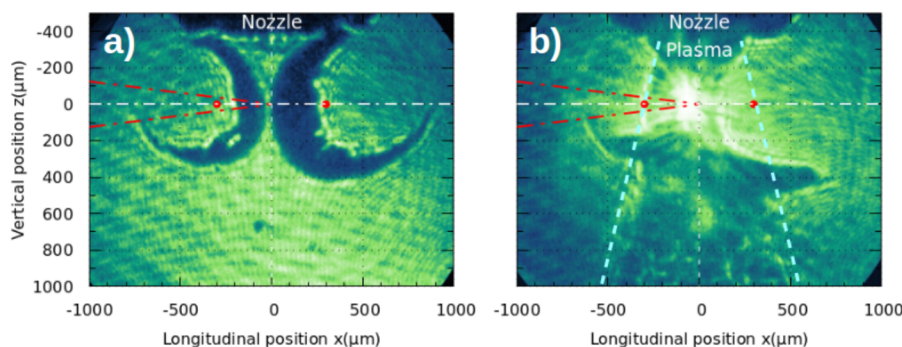**FIG. 8.** 2D space-resolved (GOI snapshot) shadowgraphs of the plasma tailored on the two opposite sides, for a gas jet backing pressure of 300 bars, at two different times: (a) before the collision of the HSWs; (b) just after their collision and the arrival of the ps pulse. The blue dashed lines indicate the edges of the shadowgraph measured without plasma tailoring (Fig. 2). The vertical scale is the same for both images.

axis, where the plasma has been expelled by the HSWs, the ps pulse does not create any additional perturbation of the shadowgraph, indicating that it propagates almost freely, up to the HSW-collision region, where it encounters a high-density plasma slab and generates second-harmonic emission (near $x \sim -100\ \mu m$).

Examples of proton spectra obtained by tailoring the gas jet from the two opposite sides are presented in Fig. 9. The maximum energy and the shape of the spectra at 70° are similar to those obtained without tailoring (Fig. 4). However, despite the shot-to-shot fluctuations, the tendency observed when tailoring only the entrance side (Fig. 6) is enhanced when both sides are tailored: the acceleration in the forward direction is improved, and the energy distribution becomes more peaked. At 30°, the portion of the spectrum induced by CSA moves toward higher energies and is now clearly separated from the low-energy thermal part. The maximum energy is more than doubled, reaching 3.2 MeV.

The number of protons accelerated above 1 MeV is also significantly increased at 0° and 30°. Comparison with the single-HSW case (Fig. 6) demonstrates that the improvement in acceleration is not only the result of a better propagation of the ps pulse at the plasma entrance. Compared with the case without tailoring at 800 bars (Fig. 4), the number of protons accelerated at 70° is similar or larger, despite a lower backing pressure of 200–300 bars. This indicates that the collision of the HSWs has compensated for the initially lower plasma density (the expected total compression factor[48] is $\gtrsim 8$) and enabled a value at least equivalent to that at 800 bars to be reached, close to n_c. Not only does this increase the number of protons available in the plasma but, by increasing the plasma density, it helps to increase the ps-pulse absorption[58,59] and thus the velocity of the collisionless shockwave and the maximum proton energies. Let us note that the lower backing pressure used for the tailoring cases was chosen to avoid refraction of the ns beam at the jet entrance and enable better plasma expulsion by the HSW, while preserving the high density at the jet center thanks to the collision of the HSWs.[48]

Very similar results were obtained in the GSI experiment. A 2D shadowgraph at the collision of the two HSWs is presented in Fig. 10(a). The croissant-like shape of the HSWs is more square. This is due to the square shape of the wings of the ns-beam focal spots. Despite this difference, the sharpness and the width (~200 μm) of the

plasma slab are very similar to those in the LULI experiment. The proton spectrum measured at 53° and associated with the interaction of the ps pulse with this plasma slab is presented in Fig. 10(b). As in the LULI experiment, the spectrum has a low-energy exponential distribution without tailoring (<2 MeV), evolving to a peaked distribution at higher energies, up to 5.5 MeV, when two-sided tailoring is applied. Compared with the LULI experiment, the laser intensity was a factor of about four larger on GSI ($a_0 \sim 8$ instead of 4), leading as expected to an approximate doubling of the maximum energy of the protons.

Part of the shot-to-shot fluctuations observed on both experiments comes from variations on the plasma profile at the ps-pulse arrival, which can significantly affect the quality (uniformity, angle, and Mach number) of the collisionless shockwave. These variations originate mainly from fluctuations in the dynamics of the HSWs, which are sensitive to (i) the energy in the wing of the ns-beam focal spot (see Sec. VI) and (ii) the exact position of the focal spot on the edge of the gas jet density profile. For example, from the expression for $n_{atom}(r)$ given in Sec. II, there is a factor-of-3.6 difference in density between $r = 250\ \mu m$ and $r = 350\ \mu m$. This induces an order-of-magnitude difference in the inverse bremsstrahlung absorption ($K_{BI} \propto n_e^2$) and thus in the amplitude and velocity of each HSW, leading to variations in the time of collision as well as in the position, density, width, and shape of the final plasma slab encountered by the ps pulse. Another part of the fluctuations comes from the hosing instability,[60] which modifies the direction of propagation of the ps pulse, and which is particularly strong in near-critical plasmas. This laser beam instability ultimately leads to fluctuations in the direction of the collisionless shock and of the proton beam. It affects more significantly the detection in the forward direction, which is mainly sensitive to CSA.

Table I summarizes the number of accelerated protons and the energy of the proton beam for the LULI spectra of Figs. 4, 6, and 9 associated with the three tailoring scenarios. Despite the relatively strong shot-to-shot fluctuations, the result in the table demonstrate that tailoring the plasma from the two opposite sides improves the acceleration toward the laser direction, in terms of the number of protons as well as of the energy of the proton beam. The optimal acceleration in the forward direction also corresponds to the
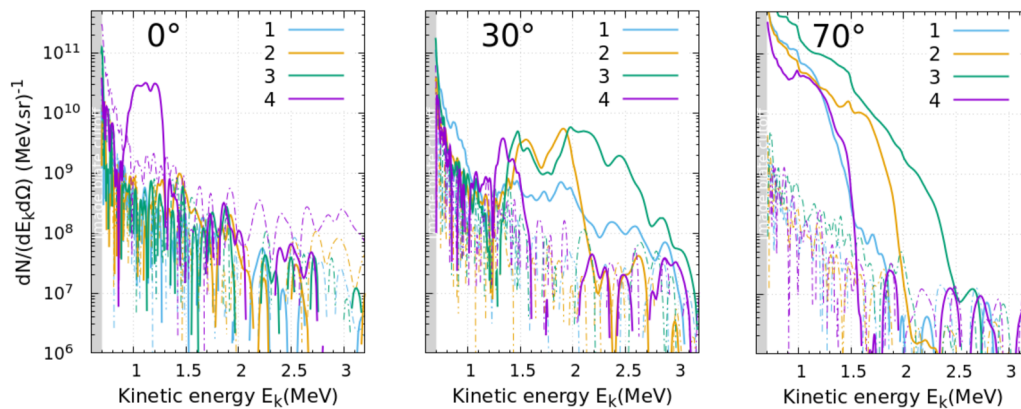

FIG. 9. Proton spectra from four laser shots on the LULI experiment, in the case of a plasma tailored on both sides (as in Fig. 7), and a gas jet backing pressure of 300 bars on shot 1 and 200 bars on shots 2, 3, and 4. The dashed lines show the noise level of each spectrum. The vertical scale is the same for all three graphs.
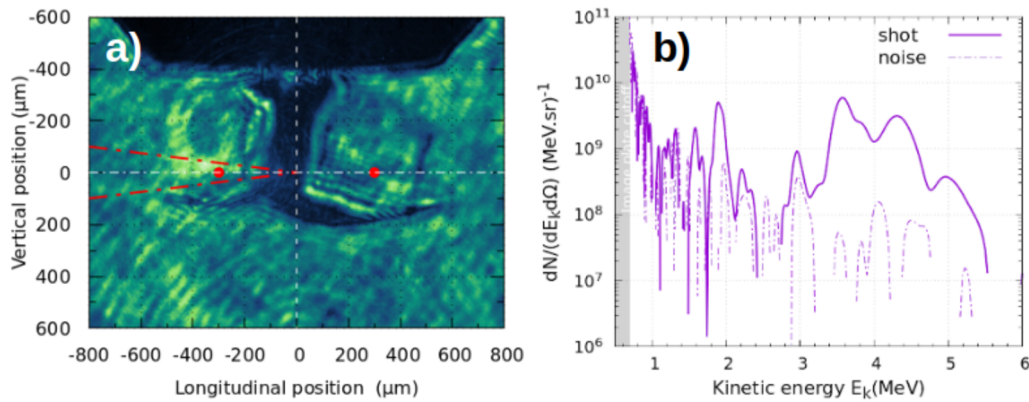
FIG. 10. Typical result from the GSI experiment: (a) 2D space-resolved (GOI snapshot) shadowgraph of the plasma tailored on both sides; (b) associated proton spectrum measured at 50°. The gas jet backing pressure was 100 bars. The shadowgraph is 40 ps before the ps-pulse arrival.

minimum transverse acceleration (the last line in Table I). Only one shot is presented for the one-sided case. Nevertheless, several shots with one-sided tailoring were performed in the GSI experiment. They confirm the evolution of the acceleration observed in the LULI experiment between no tailoring, one-sided tailoring, and two-sided tailoring. The energy cutoff $E_k > 1$ MeV used in Table I artificially sets to zero the signal observed in the forward direction without tailoring. However, the associated spectra [Figs. 4(a) and 4(b)] are broad and at very low energy, below 1 MeV at 0° and 1.1 MeV at 30°. The cutoff at 1 MeV thus appears to be a reasonable

value to distinguish forward acceleration by CSA (peaked spectrum) from ponderomotive acceleration.

Despite the shot-to-shot fluctuations, all the improvements observed in the proton spectra indicate that the laser-plasma conditions become closer to those required for efficient CSA,[13,14] namely, (i) a near-critical plasma density to get efficient laser absorption of the ps pulse and thus strong plasma heating (MeV), (ii) a narrow plasma length to favor uniform heating, leading to a uniform shock velocity and thus the production of monoenergetic protons, and (iii) an exponentially decreasing output density gradient to get

TABLE I. Number of protons and total energy of the spectra for $E_k > 1$ MeV, measured at angles of 0°, 30°, and 70°, and for the different configurations of plasma tailoring. Obtained by integrating the spectra of Figs. 4, 6, and 9 between $E_k = 1$ and 3.5 MeV. Acceleration in the forward direction is highlighted in yellow.

	dN/dΩ			dE/dΩ			P(bars)
Angle (°)	0	30	70	0	30	70	/
No tailoring (Fig. 3)	0	4.1	28	0	4	36	800
	0	0	181	0	0	220	800
	0	0	15	0	0	18	600
	0	0	73	0	0	91	450
	0	0	97	0	0	109	400
One side (Fig. 5)	2.4	6.4	5.6	2.9	7.1	6.6	200
Two sides (Fig. 8)	0.44	5.2	131	0.25	9	146	300
	1.7	19	162	1.9	32	203	200
	1.1	33	516	1.6	64	645	200
	65	5.7	99	70	7.5	114	200

a uniform sheath field that preserves the monoenergetic distribution as protons are reflected by the shock.

The proton energy expected from CSA[13,14] is of the order of E_k (MeV) $\sim 2M^2 T_e$ (MeV), where M is the Mach number of the collisionless wave and T_e (MeV) $\sim 0.078(\eta/\alpha)a_0\tau$ (ps)$/L$ (mm), with τ the duration of the laser pulse, η its absorption efficiency, $\alpha = 3/2$ for nonrelativistic plasmas ($T_e \ll m_e c^2$), and $\alpha = 3$ in the relativistic case. The absorption efficiency depends on a_0 and n_e. In our conditions, it is expected[14,49,58,59] to be between 0.25 and 0.5. Taking $\alpha = 2.2$ and assuming 0.05 mm $< L <$ 0.1 mm (smaller than the shadowgraph size; see Sec. VI), T_e is expected to be of the order of 0.35–1.4 MeV on both the LULI and the GSI experiments (same $a_0\tau$). Taking for M the minimum value required for the shock to reflect protons,[14,61] $M = M_{cr} \sim 1.6$, leads to expected proton energies of 1.8 MeV $< E_k <$ 7.2 MeV, in good agreement with our measurements.

As discussed in Sec. I, the maximum proton energy from CSA driven by a $\lambda_0 = 1$ μm laser is expected[13,14] to occur for a plasma length close to $L_{opt} \sim 40$ μm. The width of the plasma observed in Figs. 7, 8, and 10(a) appears to be $\sim$200–300 μm. However, the width of the shadowgraph could significantly overestimate that of the density profile. For example, the gas jet FWHM is $\sim$270 μm, while on Figs. 2 and 3, the full width of the shadowgraph is $\sim$600–800 μm, representing the very low wing of the density profile, 0.08–0.025 of the density at the jet center. The plasma slab at the collision of the HSWs can thus be much narrower than its apparent size on the shadowgraph.

VI. PLASMA TAILORING: COMPARISON WITH NUMERICAL SIMULATIONS

The CSA depends strongly on the plasma length L. Our previous numerical study[48] indicated that the width of the density profile at the collision of the two HSWs was below or of the order of tens of micrometers, while, as previously mentioned, the dark part of the shadowgraphs in Figs. 7 and 10(a) is 200–300 μm wide. This dark part originates from light rays that are so refracted by the density gradient that they are not collected by the lens of the imaging system. This width thus depends on the aperture of the diagnostic (3.5° on the LULI experiment and 2° on GSI) and can be significantly larger than the FWHM of the density profile. In other words, when strong refraction occurs (our conditions), for a defined density profile, the width of the shadowgraph does not directly reproduce the width of the profile, but results from the amplitude of the density
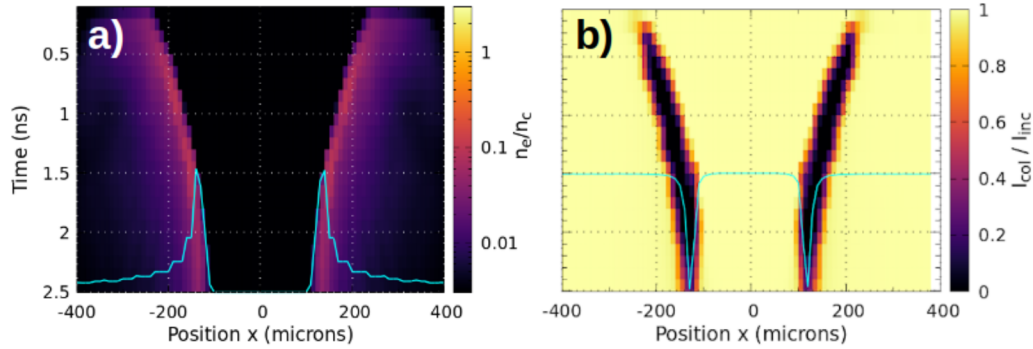

FIG. 11. (a) Temporal evolution of the density profile along the ps-beam axis from 3D TROLL simulations. The two ns beams are focused 300 μm from both sides of the gas jet center. The initial maximum plasma density (at $x = 0$) is $n_e^0 = 2 \times 10^{20}$ cm^{-3} ($= n_c/5$). The spatial intensity profile of the ns beams is $I(r) = 5.4 \times 10^{14} \exp[-(r/25)^2]$, and the energy in each beam is 6 J. (b) Post-processing of the shadowgraphy diagnostic from the TROLL outputs. The cyan lineouts are density and shadowgraph profiles at $t = 2.5$ ns.
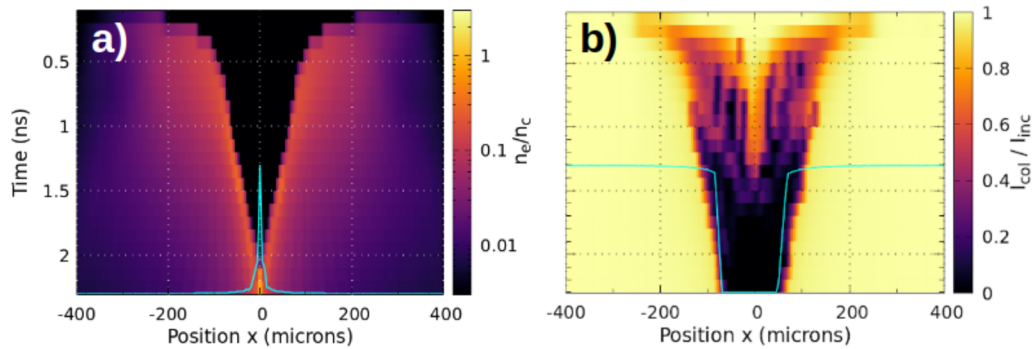

FIG. 12. Same as Fig. 11, but for a spatial profile of the ns beams with a low-intensity wing: $I(r) = 3 \times 10^{14}\{\exp[-(r/25)^2] + 0.0172\exp[-(r/110)^2]\}$ (W/cm^2) and 4.5 J in each beam. The cyan lineouts are density and shadowgraph profiles at $t = 2.3$ ns.

gradient and the diagnostic aperture. The smaller the lens aperture, the larger is the dark part of the shadowgraph. To estimate for our experimental parameters the width ratio between the density profile and the dark part of the shadowgraph, we performed 3D hydrodynamics simulations and post-processed the probe beam propagation (refraction and inverse bremsstrahlung absorption) to simulate the shadowgraphy diagnostic. As in our previous study,[48] we used the radiation-hydrodynamics code TROLL,[62] but in a 3D geometry, allowing to use as inputs the experimentally measured 3D density profile of the gas jet. We also used the experimental temporal profile of the ns beams. Figure 11(a) shows the temporal evolution of the density profile along the ps-beam axis. As already detailed in Ref. 48, each of the two ns beams, focused 300 μm from both sides of the gas jet center ($x = 0$) generates a HSW. Only the part of the cylindrical HSW that converges toward the gas jet center leads to a high density jump, while the part traveling toward vacuum is not visible because of its quick spread and decrease in amplitude. The initial maximum plasma density (at $x = 0$) is $n_e^0 = 2 \times 10^{20}$ cm^{-3} ($= n_c/5$), as for the shot presented in Fig. 7(a). The spatial intensity profile of the ns beams is a Gaussian of 25 μm radius. Figure 11(b) is the simulation of the shadowgraphy diagnostic. Compared with Fig. 7(a), after 2.5 ns, the HSWs have still not reached the gas jet center. Also, at the HSW creation, the experimental shadowgraph has a large horizontal shape, while the simulated one is much more localized (narrow). In the experiment, the laser intensity profile did not in fact consist of just a narrow high-intensity part, but also had a lower-intensity wing: $I(r) = 3 \times 10^{14}\{\exp[-(r/25)^2] + 0.0172 \exp[-(r/110)^2]\}$ W/cm^2. Despite its lower intensity, this large wing contained ~25% of the laser energy—enough to contribute to the HSW excitation. Figure 12 shows the evolution of the density profile and of the associated shadowgraph when the wing of the ns beams is taken into account, and for the same laser energy (4.5 J in each beam) as the shot in Fig. 7. The simulated shadowgraph is very similar to the experimental one [Fig. 7(a)], reproducing the initial "horizontal" part followed by two large traces that converge when the two HSWs collide after ~2.3 ns, at the jet center. The effect of the wing of the focal spot on the HSW evolution is also illustrated in Fig. 13, which compares the profiles of (a) the laser focal spot, (b) the electron temperature, and (c) the electron density for the cases without (left) and with (right) the wing. Even though

the intensity is higher without the wing, because the energy deposition is more localized, the HSWs start with a smaller diameter and farther from the jet center, making their collision impossible. With the wing, the HSWs are generated with a larger diameter, enabling them to reach the jet center faster. A point to underline here is that the density deepening at the edge of the jet is nevertheless[1–62] more efficient without the wing (there is more localized energy deposition), as can also be observed on comparing Figs. 11(a) and 12(a). Figure 13(c) also shows that the simulations reproduce very well the croissant-like shape observed experimentally (Figs. 5, 7, 8, and 10). The influence of the wing is also observed in Fig. 10(a), where the square shape of the GSI ns beams is retrieved in the shape of the HSWs.

Let us note that since the hydrogen is very rapidly ionized, full ionization was imposed at the beginning of the simulation and, to avoid an early gas jet expansion, an initial temperature of 300 K was imposed. This has no effect on the plasma evolution induced by the ns beams. However, in the regions not affected by these beams or by the HSWs they produce, where the medium should still be in its gaseous state, its refractive index as well as the inverse bremsstrahlung absorption of the low-intensity probe beam are strongly overestimated. To avoid this artifact, in the post-processing of the shadowgraphy diagnostics, the ionization state was corrected using the Saha ionization equation. The density map presented in Fig. 11(a) includes this correction. Without correction, the shadowgraph at early times is completely dark at the jet center, while the gas is still not ionized and should fully transmit the probe beam (as experimentally observed and mentioned in Secs. IV and V).

The normalized lineouts in Figs. 12(a) and 12(b) show respectively the density and shadowgraph profiles at the collision time ($t = 2.3$ ns). The width of the shadowgraph is ~150 μm, which is much larger than the width of the plasma slab, $\lesssim$20 μm. Applying this same factor difference to the experimental shadowgraphs would indicate that the plasma slab at the collision time was 30–40 μm thick, similar to the predicted optimal value L_{opt} for CSA (Sec. I).

From Fig. 12(a), the peak density at the collision time is ~$3n_c$. By conservation of particle number, if the experimental plasma slab is of the order of or more than twice the thickness in the simulations, the peak density should be lower by this same factor, of the order of or less than $1.5n_c$.

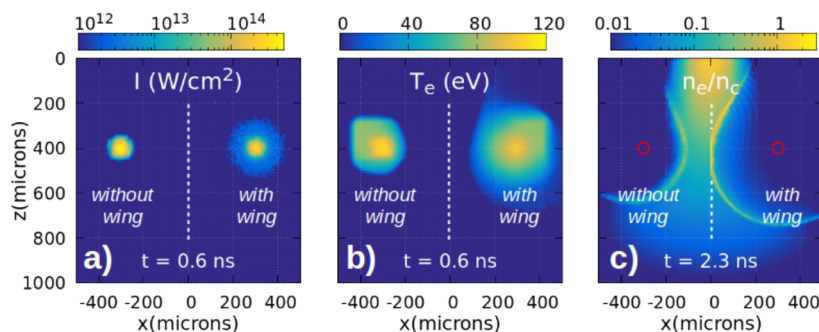**FIG. 13.** Spatial profiles of (a) the laser focal spot, (b) the electron temperature, (c) the electron density for the case without the wing in the intensity profile (left, Fig. 11) and with the wing (right, Fig. 12). (a) and (b) Are at 0.6 ns, the maximum of the laser, and (c) is at 2.3 ns (the time at which the HSWs collide in the case with the wing). The vertical scale is the same for all three images.

VII. DISCUSSION

Even if the thickness of the plasma slab is close to optimal, its density needs also to be adjusted to an optimal value that depends on the laser intensity. To drive a strong collisionless shock and accelerate ions at high energies, high laser absorption is required (see Sec. V), which implies $n_e \sim \gamma n_c$. With $a_0 \sim 4$ at LULI and 8 at GSI, this leads to $n_e/n_c \sim 3$ and 5.7, respectively. Our previous numerical study[49] also showed that the maximum proton energy drops quickly below this optimal value. The density of the plasma slab was thus probably too low for optimal proton acceleration. An easy way to produce plasma slabs of higher density is to increase the backing pressure of the gas jet, as long as the residual density in the wing of the slab does not disturb the propagation of the ps laser beam.

The efficiency of the acceleration depends not only on the intensity of the ps laser, but also on the size of its focal spot.[14] The shock width (which is close to the laser spot size W_0) has to be large enough that the plasma, expanding transversely at the sound speed, does not leave the shock region before the acceleration occurs. Assuming an isothermal expansion, this condition yields $W_0 \gtrsim L/M$. Taking for M the minimum value required for the shock to reflect protons, $M_{cr} = 1.6$, and $L = 40$ μm leads to $W_0 \gtrsim 25$ μm. The focal spot on the LULI and GSI experiments (FWHM ~10 μm) was thus probably too small for an optimal acceleration. With a larger focal spot, the shape of the shock will be flatter, favoring forward acceleration, at higher energy. The larger surface might also increase the number of accelerated protons.

The clearly peaked spectra observed with the two-sided tailoring indicate that even if the plasma slab is relatively narrow, the density gradient at its backside is not very sharp, avoiding TNSA, and presenting a "slowly" decreasing profile with a small and constant sheath electric field, favoring monoenergetic acceleration.[13]

VIII. CONCLUSIONS

We recently proposed a new technique of plasma tailoring by laser-driven hydrodynamic shockwaves generated on both sides of a gas jet. In a continuation of this numerical work, we have studied experimentally the influence of the tailoring on proton acceleration driven by a high-intensity ps laser in three cases: without tailoring, by tailoring only the entrance side of the ps laser, and by tailoring both sides of the gas jet. Without tailoring, the acceleration is transverse to the laser axis, with a low-energy exponential spectrum, produced by Coulomb explosion. When the front side of the gas jet is tailored, a forward acceleration appears, which is significantly enhanced when both the front and back sides of the plasma are tailored. This forward acceleration produces higher-energy protons (up to 5.5 MeV), with a peaked spectrum, and is in good agreement with the mechanism of CSA. The total number of accelerated protons is also enhanced by this two-sided tailoring. The spatiotemporal evolution of the plasma profile as been characterized by optical shadowgraphy of a probe beam. The refraction and absorption of this beam have been simulated by post-processing 3D hydrodynamic simulations of the plasma tailoring. The dynamics of the hydrodynamic shockwaves are reproduced well only if the low-intensity wing in the focal spot of the tailoring beams is taken into account. Comparison of the simulated shadowgraphs with the experimental ones has allowed estimation of the thickness (~30–40 μm) and density (~1.5n_c) of the plasma slab produced by tailoring both sides of the gas jet. These values are close to those required to trigger CSA. However, the shot-to-shot fluctuations of the forward proton beam indicate that the set of criteria for optimal CSA have still not been reached. Improving the focal spot quality of the tailoring ns beams and increasing the backing pressure of the gas jet as well as the focal spot size of the ps beam would enable a more stable CSA to be reached, as well as the generation of a proton beam with a larger number of protons, at higher energy, and of lower spectral width and emittance.

AUTHOR DECLARATIONS

Conflict of Interest

The authors have no conflicts to disclose.

Author Contributions

J.-R. Marquès: Writing – original draft (lead). **L. Lancia**: Conceptualization (supporting); Methodology (equal); Project administration (lead); Validation (equal); Writing – review & editing (equal). **P. Loiseau**: Conceptualization (equal); Software (lead); Validation (equal); Writing – review & editing (equal). **P. Forestier-Colleoni**: Methodology (supporting); Validation (supporting); Writing – review & editing (supporting). **M. Tarisien**: Conceptualization (supporting); Methodology (supporting); Writing – review & editing (supporting). **E. Atukpor**: Methodology (supporting). **V. Bagnoud**: Project administration (supporting); Writing – review & editing (equal). **C. Brabetz**: Conceptualization (supporting); Methodology (supporting); Writing – review & editing (supporting). **F. Consoli**: Methodology (supporting); Writing – review & editing (supporting). **J. Domange**: Methodology (equal); Writing – review & editing (supporting). **F. Hannachi**: Methodology (supporting); Writing – review & editing (equal). **P. Nicolaï**: Writing – review & editing (supporting). **M. Salvadori**: Methodology (supporting); Resources (supporting); Writing – review & editing (supporting). **B. Zielbauer**: Methodology (supporting); Resources (supporting); Writing – review & editing (supporting).

DATA AVAILABILITY

The data that support the findings of this study are available from the corresponding author upon reasonable request.

REFERENCES

[1] R. Blandford and D. Eichler, "Particle acceleration at astrophysical shocks: A theory of cosmic ray origin," Phys. Rep. **154**, 1 (1987).

[2] F. C. Jones and D. C. Ellison, "The plasma physics of shock acceleration," Space Sci. Rev. **58**, 259 (1991).

[3] D. Caprioli, P. Blasi, and E. Amato, "Non-linear diffusive acceleration of heavy nuclei in supernova remnant shocks," Astropart. Phys. **34**, 447 (2011).

[4] K. Koyama, R. Petre, E. V. Gotthelf, U. Hwang, M. Matsuura, M. Ozaki, and S. S. Holt, "Evidence for shock acceleration of high-energy electrons in the supernova remnant SN1006," Nature **378**, 255 (1995).

[5] O. Adriani, G. C. Barbarino, G. A. Bazilevskaya, R. Bellotti, M. Boezio, E. A. Bogomolov, L. Bonechi, M. Bongi, V. Bonvicini, S. Borisov, S. Bottai, A. Bruno, F. Cafagna, D. Campana, R. Carbone, P. Carlson, M. Casolino, G. Castellini, L. Consiglio, M. P. De Pascale, C. De Santis, N. De Simone, V. Di Felice, A. M. Galper, W. Gillard, L. Grishantseva, G. Jerse, A. V. Karelin, S. V. Koldashov, S. Y. Krutkov, A. N. Kvashnin, A. Leonov, V. Malakhov, V. Malvezzi, L. Marcelli, A. G. Mayorov, W. Menn, V. V. Mikhailov, E. Mocchiutti, A. Monaco, N. Mori, N. Nikonov, G. Osteria, F. Palma, P. Papini, M. Pearce, P. Picozza, C. Pizzolotto, M. Ricci, S. B. Ricciarini, L. Rossetto, R. Sarkar, M. Simon, P. Spillantini, Y. I. Stozhkov, A. Vacchi, E. Vannuccini, G. Vasilyev, S. A. Voronov, Y. T. Yurkin, J. Wu, G. Zampa, N. Zampa, and V. G. Zverev, "PAMELA measurements of cosmic-ray proton and helium spectra," Science **332**, 69 (2011).

[6] A. Spitkovsky, "Particle acceleration in relativistic collisionless shocks: Fermi process at last?," Astrophys. J. **682**, L5 (2008).

[7] A. Spitkovsky, "On the structure of relativistic collisionless shocks in electron-ion plasmas," Astrophys. J. **673**, L39 (2008).

[8] R. P. Drake, "The design of laboratory experiments to produce collisionless shocks of cosmic relevance," Phys. Plasmas **7**, 4690 (2000).

[9] C. Courtois, R. A. D. Grundy, A. D. Ash, D. M. Chambers, N. C. Woolsey, R. O. Dendy, and K. G. McClements, "Experiment on collisionless plasma interaction with applications to supernova remnant physics," Phys. Plasmas **11**, 3386 (2004).

[10] N. C. Woolsey, Y. A. Ali, R. G. Evans, R. A. D. Grundy, S. J. Pestehe, P. G. Carolan, N. J. Conway, R. O. Dendy, P. Helander, K. G. McClements, J. G. Kirk, P. A. Norreys, M. M. Notley, and S. J. Rose, "Collisionless shock and supernova remnant simulations on VULCAN," Phys. Plasmas **8**, 2439 (2001).

[11] F. Fiuza, G. F. Swadling, A. Grassi, H. G. Rinderknecht, D. P. Higginson, D. D. Ryutov, C. Bruulsema, R. P. Drake, S. Funk, S. Glenzer, G. Gregori, C. K. Li, B. B. Pollock, B. A. Remington, J. S. Ross, W. Rozmus, Y. Sakawa, A. Spitkovsky, S. Wilks, and H.-S. Park, "Electron acceleration in laboratory-produced turbulent collisionless shocks," Nat. Phys. **16**, 916–920 (2020).

[12] L. O. Silva, M. Marti, J. R. Davies, R. A. Fonseca, C. Ren, F. S. Tsung, and W. B. Mori, "Proton shock acceleration in laser–plasma interactions," Phys. Rev. Lett. **92**, 015002 (2004).

[13] F. F. Fiuza, A. Stockem, E. Boella, R. A. Fonseca, L. O. Silva, D. Haberberger, S. Tochitsky, C. Gong, W. B. Mori, and C. Joshi, "Laser-driven shock acceleration of monoenergetic ion beams," Phys. Rev. Lett. **109**, 215001 (2012).

[14] F. F. Fiuza, A. Stockem, E. Boella, R. A. Fonseca, L. O. Silva, D. Haberberger, S. Tochitsky, W. B. Mori, and C. Joshi, "Ion acceleration from laser-driven electrostatic shocks," Phys. Plasmas **20**, 056304 (2013).

[15] C. A. J. Palmer, N. P. Dover, I. Pogorelsky, M. Babzien, G. I. Dudnikova, M. Ispiriyan, M. N. Polyanskiy, J. Schreiber, P. Shkolnikov, V. Yakimenko, and Z. Najmudin, "Monoenergetic proton beams accelerated by a radiation pressure driven shock," Phys. Rev. Lett. **106**, 014801 (2011).

[16] S. Bulanov, T. Esirkepov, P. Migliozzi, F. Pegoraro, T. Tajima, and F. Terranova, "Neutrino oscillation studies with laser-driven beam dump facilities," Nucl. Instrum. Methods Phys. Res., Sect. A **540**, 25 (2005).

[17] M. Roth, T. E. Cowan, M. H. Key, S. P. Hatchett, C. Brown, W. Fountain, J. Johnson, D. M. Pennington, R. A. Snavely, S. C. Wilks, K. Yasuike, H. Ruhl, F. Pegoraro, S. V. Bulanov, E. M. Campbell, M. D. Perry, and H. Powell, "Fast ignition by intense laser-accelerated proton beams," Phys. Rev. Lett. **86**, 436 (2001).

[18] M. Temporal, R. Ramis, J. J. Honrubia, and S. Atzeni, "Fast ignition induced by shocks generated by laser-accelerated proton beams," Plasma Phys. Controlled Fusion **51**, 035010 (2009).

[19] M. Temporal, J. J. Honrubia, and S. Atzeni, "Numerical study of fast ignition of ablatively imploded deuterium–tritium fusion capsules by ultra-intense proton beams," Phys. Plasmas **9**, 3098 (2002).

[20] F. P. Boody, R. Hopfl, H. Hora, and J. C. Kelly, "Laser-driven ion source for reduced-cost implantation of metal ions for strong reduction of dry friction and increased durability," Laser Part. Beams **14**, 443 (1996).

[21] M. Borghesi, D. H. Campbell, A. Schiavi, M. G. Haines, O. Willi, A. J. MacKinnon, P. Patel, L. A. Gizzi, M. Galimberti, R. J. Clarke, F. Pegoraro, H. Ruhl, and S. Bulanov, "Electric field detection in laser–plasma interaction experiments via the proton imaging technique," Phys. Plasmas **9**, 2214 (2002).

[22] C. K. Li, F. H. Séguin, J. A. Frenje, J. R. Rygg, R. D. Petrasso, R. P. J. Town, P. A. Amendt, S. P. Hatchett, O. L. Landen, A. J. Mackinnon, P. K. Patel, V. A. Smalyuk, T. C. Sangster, and J. P. Knauer, "Measuring E and B fields in laser-produced plasmas with monoenergetic proton radiography," Phys. Rev. Lett. **97**, 135003 (2006).

[23] L. Romagnani, S. V. Bulanov, M. Borghesi, P. Audebert, J. C. Gauthier, K. Löwenbrück, A. J. Mackinnon, P. Patel, G. Pretzler, T. Toncian, and O. Willi, "Observation of collisionless shocks in laser–plasma experiments," Phys. Rev. Lett. **101**, 025004 (2008).

[24] S. V. Bulanov, T. Z. Esirkepov, V. S. Khoroshkov, A. Kuznetsov, and F. Pegoraro, "Oncological hadrontherapy with laser ion accelerators," Phys. Lett. A **299**, 240 (2002).

[25] S. V. Bulanov and V. S. Khoroshkov, "Feasibility of using laser ion accelerators in proton therapy," Plasma Phys. Rep. **28**(5), 453 (2002).

[26] V. Malka, S. Fritzler, E. Lefebvre, E. d'Humières, R. Ferrand, G. Grillon, C. Albaret, S. Meyroneinc, J. P. Chambaret, A. Antonetti, and D. Hulin, "Practicability of protontherapy using compact laser systems," Med. Phys. **31**, 1587 (2004).

[27] L. Karsch, E. Beyreuther, W. Enghardt, M. Gotz, U. Masood, U. Schramm, K. Zeil, and J. Pawelke, "Towards ion beam therapy based on laser plasma accelerators," Acta Oncol. **56**(11), 1359 (2017).

[28] I. Spencer, K. Ledingham, R. Singhal, T. McCanny, P. McKenna, E. Clark, K. Krushelnick, M. Zepf, F. Beg, M. Tatarakis, A. Dangor, P. Norreys, R. Clarke, R. Allott, and I. Ross, "Laser generation of proton beams for the production of short-lived positron emitting radioisotopes," Nucl. Instrum. Methods Phys. Res., Sect. B **183**, 449 (2001).

[29] E. Lefebvre, E. D'Humières, S. Fritzler, and V. Malka, "Numerical simulation of isotope production for positron emission tomography with laser-accelerated ions," J. Appl. Phys. **100**, 113308 (2006).

[30] R. A. Snavely, M. H. Key, S. P. Hatchett, T. E. Cowan, M. Roth, T. W. Phillips, M. A. Stoyer, E. A. Henry, T. C. Sangster, M. S. Singh, S. C. Wilks, A. MacKinnon, A. Offenberger, D. M. Pennington, K. Yasuike, A. B. Langdon, B. F. Lasinski, J. Johnson, M. D. Perry, and E. M. Campbell, "Intense high-energy proton beams from petawatt-laser irradiation of solids," Phys. Rev. Lett. **85**, 2945 (2000).

[31] S. C. Wilks, A. B. Langdon, T. E. Cowan, M. Roth, M. Singh, S. Hatchett, M. H. Key, D. Pennington, A. MacKinnon, and R. A. Snavely, "Energetic proton generation in ultra-intense laser–solid interactions," Phys. Plasmas **8**, 542 (2001).

[32] T. Esirkepov, M. Borghesi, S. V. Bulanov, G. Mourou, and T. Tajima, "Highly efficient relativistic-ion generation in the laser-piston regime," Phys. Rev. Lett. **92**, 175003 (2004).

[33] A. P. L. Robinson, M. Zepf, S. Kar, R. G. Evans, and C. Bellei, "Radiation pressure acceleration of thin foils with circularly polarized laser pulses," New J. Phys. **10**, 013021 (2008).

[34] A. Macchi, S. Veghini, and F. Pegoraro, "Light sail acceleration reexamined," Phys. Rev. Lett. **103**, 085003 (2009).

[35] B. Qiao, S. Kar, M. Geissler, P. Gibbon, M. Zepf, and M. Borghesi, "Dominance of radiation pressure in ion acceleration with linearly polarized pulses at intensities of 10^{21} W cm^{-2}," Phys. Rev. Lett. **100**, 115002 (2012).

[36] L. Yin, B. J. Albright, B. M. Hegelich, K. J. Bowers, K. A. Flippo, T. J. T. Kwan, and J. C. Fernandez, "Monoenergetic and GeV ion acceleration from the laser breakout afterburner using ultrathin targets," Phys. Plasmas **14**, 056706 (2007).

[37] A. Henig, D. Kiefer, K. Markey, D. C. Gautier, K. A. Flippo, S. Letzring, R. P. Johnson, T. Shimada, L. Yin, B. J. Albright, K. J. Bowers, J. C. Fernandez, S. G. Rykovanov, H.-C. Wu, M. Zepf, D. Jung, V. K. Liechtenstein, J. Schreiber, D. Habs, and B. M. Hegelich, "Enhanced laser-driven ion acceleration in the relativistic transparency regime," Phys. Rev. Lett. **103**, 045002 (2009).

[38]T. Nakamura, S. V. Bulanov, T. Z. Esirkepov, and M. Kando, "High-energy ions from near-critical density plasmas via magnetic vortex acceleration," Phys. Rev. Lett. **105**, 135002 (2010).

[39]J. Park, S. S. Bulanov, J. Bin, Q. Ji, S. Steinke, J. L. Vay, C. G. R. Geddes, C. B. Schroeder, W. P. Leemans, T. Schenkel, and E. Esarey, "Ion acceleration in laser generated megatesla magnetic vortex," Phys. Plasmas **26**, 103108 (2019).

[40]Z. Najmudin, C. A. J. Palmer, N. P. Dover, I. Pogorelsky, M. Babzien, A. E. Dangor, G. I. Dudnikova, P. S. Foster, J. S. Green, M. Ispiriyan, D. Neely, M. N. Polyanskiy, J. Schreiber, P. Shkolnikov, and V. Yakimenko, "Observation of impurity free monoenergetic proton beams from the interaction of a CO_2 laser with a gaseous target," Phys. Plasmas **18**, 056705 (2011).

[41]D. Haberberger, S. Tochitsky, F. Fiuza, C. Gong, R. A. Fonseca, L. Silva, W. B. Mori, and C. Joshi, "Collisionless shocks in laser-produced plasma generate monoenergetic high-energy proton beams," Nat. Phys. **8**, 95 (2012).

[42]O. Tresca, N. P. Dover, N. Cook, C. Maharjan, M. N. Polyanskiy, Z. Najmudin, P. Shkolnikov, and I. Pogorelsky, "Spectral modification of shock accelerated ions using a hydrodynamically shaped gas target," Phys. Rev. Lett. **115**, 094802 (2015).

[43]Y. Chen, M. Helle, A. Ting, D. Gordon, N. Dover, O. Ettlinger, Z. Najmudin, M. Polyanskiy, I. Pogorelsky, and M. Babzien, "Laser acceleration of protons with an optically shaped, near-critical hydrogen gas target," AIP Conf. Proc **1812**, 090002 (2017).

[44]S. N. Chen, M. Vranic, T. Gangolf, E. Boella, M. Antici, M. Bailly-Grandvaux, P. Loiseau, H. Pépin, G. Revet, J. J. Santos, A. M. Schroer, M. Starodubtsev, O. Willi, L. O. Silva, E. d'Humières, and J. Fuchs, "Collimated protons accelerated from an overdense gas jet irradiated by a 1 μm wavelength high-intensity short-pulse laser," Sci. Rep. **7**, 13505 (2017).

[45]P. Puyuelo-Valdes, J. L. Henares, F. Hannachi, T. Ceccotti, J. Domange, M. Ehret, E. d'Humières, L. Lancia, J.-R. Marquès, X. Ribeyre, J. J. Santos, V. Tikhonchuk, and M. Tarisien, "Proton acceleration by collisionless shocks using a supersonic H_2 gas-jet target and high-power infrared laser pulses," Phys. Plasmas **26**, 123109 (2019).

[46]A. Pak, S. Kerr, N. Lemos, A. Link, P. Patel, F. Albert, L. Divol, B. B. Pollock, D. Haberberger, D. Froula, M. Gauthier, S. H. Glenzer, A. Longman, L. Manzoor, R. Fedosejevs, S. Tochitsky, C. Joshi, and F. Fiuza, "Collisionless shock acceleration of narrow energy spread ion beams from mixed species plasmas using 1 μm lasers," Phys. Rev. Accel. Beams **21**, 103401 (2018).

[47]S. Tochitsky, A. Pak, F. Fiuza, D. Haberberger, N. Lemos, A. Link, D. H. Froula, and C. Joshi, "Laser-driven collisionless shock acceleration of ions from near-critical plasmas," Phys. Plasmas **27**, 083102 (2020).

[48]J.-R. Marquès, P. Loiseau, J. Bonvalet, M. Tarisien, E. d'Humières, J. Domange, F. Hannachi, L. Lancia, O. Larroche, P. Nicolaï, P. Puyuelo-Valdes, L. Romagnani, J. Santos, and V. Tikhonchuk, "Over-critical sharp-gradient plasma slab produced by the collision of laser-induced blast-waves in a gas jet: Application to high-energy proton acceleration," Phys. Plasmas **28**, 023103 (2021).

[49]J. Bonvalet, P. Loiseau, J.-R. Marquès, E. Atukpor, E. d'Humières, J. Domange, P. Forestier-Colleoni, F. Hannachi, L. Lancia, D. Raffestin, M. Tarisien, V. Tikhonchuk, and P. Nicolaï, "Laser-driven collisionless shock acceleration of protons from gas jets tailored by one or two nanosecond beams," Phys. Plasmas **28**, 113102 (2021).

[50]J. L. Henares, P. Puyuelo-Valdes, F. Hannachi, T. Ceccotti, M. Ehret, F. Gobet, L. Lancia, J.-R. Marquès, J. J. Santos, M. Versteegen, and M. Tarisien, "Development of gas jet targets for laser–plasma experiments at near-critical density," Rev. Sci. Instrum. **90**, 063302 (2019).

[51]S. S. Bulanov, V. Y. Bychenkov, V. Chvykov, G. Kalinchenko, D. W. Litzenberg, T. Matsuoka, A. G. R. Thomas, L. Willingale, V. Yanovsky, K. Krushelnick, and A. Maksimchuk, "Generation of GeV protons from 1 PW laser interaction with near critical density targets," Phys. Plasmas **17**, 043105 (2010).

[52]J.-X. Liu, Y. Zhao, X.-P. Wang, J.-Z. Quan, T.-P. Yu, G.-B. Zhang, X.-H. Yang, Y.-Y. Ma, F.-Q. Shao, and J. Zhao, "High-flux positrons generation via two counter-propagating laser pulses irradiating near-critical-density plasmas," Phys. Plasmas **25**, 103106 (2018).

[53]X. L. Zhu, T. P. Yu, Z. M. Sheng, Y. Yin, I. C. E. Turcu, and A. Pukhov, "Dense GeV electron–positron pairs generated by lasers in near-critical-density plasmas," Nat. Commun. **7**, 13686 (2016).

[54]O. N. Rosmej, N. E. Andreev, S. Zaehter, N. Zahn, P. Christ, B. Borm, T. Radon, A. Sokolov, L. P. Pugachev, D. Khaghani, F. Horst, N. G. Borisenko, G. Sklizkov, and V. G. Pimenov, "Interaction of relativistically intense laser pulses with long-scale near critical plasmas for optimization of laser based sources of MeV electrons and gamma-rays," New J. Phys. **21**, 043044 (2019).

[55]G. S. Sarkisov, V. Y. Bychenkov, V. N. Novikov, V. T. Tikhonchuk, A. Maksimchuk, S.-Y. Chen, R. Wagner, G. Mourou, and D. Umstadter, "Self-focusing, channel formation, and high-energy ion generation in interaction of an intense short laser pulse with a he jet," Phys. Rev. E **59**, 7042 (1999).

[56]K. Krushelnick, E. L. Clark, Z. Najmudin, M. Salvati, M. I. K. Santala, M. Tatarakis, A. E. Dangor, V. Malka, D. Neely, R. Allott, and C. Danson, "Multi-MeV ion production from high-intensity laser interactions with underdense plasmas," Phys. Rev. Lett. **83**, 737 (1999).

[57]M. S. Wei, S. P. D. Mangles, Z. Najmudin, B. Walton, A. Gopal, M. Tatarakis, A. E. Dangor, E. L. Clark, R. G. Evans, S. Fritzler, R. J. Clarke, C. Hernandez-Gomez, D. Neely, W. Mori, M. Tzoufras, and K. Krushelnick, "Ion acceleration by collisionless shocks in high-intensity-laser-underdense-plasma interaction," Phys. Rev. Lett. **93**, 155003 (2004).

[58]S. C. Wilks, W. L. Kruer, M. Tabak, and A. B. Langdon, "Absorption of ultra-intense laser pulses," Phys. Rev. Lett. **69**, 1383 (1992).

[59]F. Tsung, S. Y. Tochitsky, D. J. Haberberger, W. B. Mori, and C. Joshi, "CO_2 Laser acceleration of forward directed MeV proton beams in a gas target at critical plasma density," J. Plasma Phys. **78**, 373 (2012).

[60]L. Ceurvorst, N. Ratan, M. C. Levy, M. F. Kasim, J. Sadler, R. H. H. Scott, R. M. G. M. Trines, T. W. Huang, M. Skramic, M. Vranic, L. O. Silva, and P. A. Norreys, "Mitigating the hosing instability in relativistic laser–plasma interactions," New J. Phys. **18**, 053023 (2016).

[61]R. Z. Sagdeev, "Cooperative phenomena and shock waves in collisionless plasmas," Rev. Plasma Phys. **4**, 23 (1966).

[62]E. Lefebvre, S. Bernard, C. Esnault, P. Gauthier, A. Grisollet, P. Hoch, L. Jacquet, G. Kluth, S. Laffite, S. Liberatore, I. Marmajou, P.-E. Masson-Laborde, O. Morice, and J.-L. Willien, "Development and validation of the TROLL radiation-hydrodynamics code for 3D hohlraum calculations," Nucl. Fusion **59**, 032010 (2019).